PROTEINS
STRUCTURE ■ FUNCTION ■ BIOINFORMATICS

Comparing the folding free-energy landscapes of Aβ42 variants with different aggregation properties

Simon Mitternacht,[1,2] Iskra Staneva,[1] Torleif Härd,[3] and Anders Irbäck[1]*

[1] Computational Biology and Biological Physics, Lund University, Sölvegatan 14A, SE-223 62 Lund, Sweden
[2] Department of Informatics, University of Bergen, PB 7803, N-5020 Bergen, Norway
[3] Department of Molecular Biology, Swedish University of Agricultural Sciences (SLU), Box 590, SE-751 24 Uppsala, Sweden

ABSTRACT

The properties of the amyloid-*β* peptide that lead to aggregation associated with Alzheimer's disease are not fully understood. This study aims at identifying conformational differences among four variants of full-length A*β*42 that are known to display very different aggregation properties. By extensive all-atom Monte Carlo simulations, we find that a variety of *β*-sheet structures with distinct turns are readily accessible for full-length A*β*42. In the simulations, wild type (WT) A*β*42 preferentially populates two major classes of conformations, either extended with high *β*-sheet content or more compact with lower *β*-sheet content. The three mutations studied alter the balance between these classes. Strong mutational effects are observed in a region centered at residues 23–26, where WT A*β*42 tends to form a turn. The aggregation-accelerating E22G mutation associated with early onset of Alzheimer's disease makes this turn region conformationally more diverse, whereas the aggregation-decelerating F20E mutation has the reverse effect, and the E22G/I31E mutation reduces the turn population. Comparing results for the four A*β*42 variants, we identify specific conformational properties of residues 23–26 that might play a key role in aggregation.

Proteins 2010; 78:2600–2608.

Key words: amyloid-β; mutations; all atom; implicit solvent; Monte Carlo; *J*-coupling constants; chemical shifts.

INTRODUCTION

The amyloid-β peptide is the dominant component of amyloid plaques in the brains of patients with Alzheimer's disease (AD). Understanding the formation and character of different Aβ aggregates, from oligomers to amyloid fibrils, and their roles in AD is currently the focus of intense research efforts.

Aβ is present in two major forms, Aβ40 and Aβ42, with 40 and 42 residues, respectively. Of these, Aβ42 is most strongly linked to AD. Aβ42 is also more neurotoxic[1–3] and aggregates more rapidly into oligomers, protofibrils, and fibrils.[4–7]

Some familial early-onset forms of AD are associated with single amino acid mutations of Aβ. It is well known from *in vitro* studies that such mutations can significantly alter the propensity of Aβ to aggregate. It is not obvious, however, how much one can learn from *in vitro* aggregation studies about the behavior of Aβ under complex *in vivo* conditions. This issue was recently addressed by studies of Drosophila flies expressing different Aβ42 variants.[8,9] A clear correlation was found between a variant's *in vitro* aggregation rate and its influence on fly longevity and locomotion.

A first step toward a molecular understanding of Aβ aggregation is to characterize the Aβ monomer. The solution behavior of Aβ has been studied by both NMR[10–12] and atomic-level computer simulations.[13–17] The NMR results suggest that Aβ40 and Aβ42 both are largely unstructured in aqueous solution.[10–12] The main difference seems to be that Aβ42 is more rigid than Aβ40 at the C-terminus.[12] This conclusion is supported by explicit water molecular dynamics simulations at the microsecond time scale.[16]

Another region of Aβ that might be crucial for its aggregation properties is the segment 21–30, which has been identified as a protease-resistant part of the molecule.[18] NMR[18] and computational[19–21] studies found the excised Aβ(21–30) fragment to adopt a bend structure in solution. It was further found that several familial AD mutations reduce the stability of this bend.[22,23]

Simon Mitternacht's current address is Department of Informatics, University of Bergen, PB 7803, N-5020 Bergen, Norway
*Correspondence to: A. Irbäck, Computational Biology and Biological Physics, Lund University, Sölvegatan 14A, SE-223 62 Lund, Sweden
Received 13 April 2010; Revised 12 May 2010; Accepted 14 May 2010
Published online 24 May 2010 in Wiley InterScience (www.interscience.wiley.com).
DOI: 10.1002/prot.22775

A bend in this region has also been identified in fibrils of full-length Aβ.[24,25] In the fibril models, each monomer unit has two β-strands, in Aβ40 connected by a bend at residues 25–29,[24] and in ^{35Mox}Aβ42 at residues 27–30.[25] Furthermore, a recent NMR study determined the structure of Aβ40 bound to an Affibody protein dimer and found a hairpin conformation with a turn spanning residues 24–29.[26] Sequence similarities between Affibody binders to Aβ suggest that they all recognize the same β-hairpin conformation.[27] It is therefore readily accessible and perhaps also significantly populated by monomeric Aβ in solution. In common for these fibrillar and complex-bound forms of Aβ are two β-strands that include residues 17–21 and 31–36 and a turn in between.

In addition to Aβ(21–30), there are several other Aβ fragments that have been extensively studied, both experimentally and by computer simulations. Perhaps, best studied is the strongly hydrophobic and fibril-forming[28] 7-residue fragment Aβ(16–22), which might play a driving role in the aggregation of full-length Aβ.[29] Residues 17–21 are usually called the central hydrophobic cluster (CHC).

Here in, we use implicit solvent all-atom Monte Carlo (MC) simulations to investigate the folding properties of four variants of full-length Aβ42, all of which were included in the above-mentioned Drosophila study.[9] The four variants studied are wild type (WT), the two single mutants F20E and E22G and the double mutant E22G/I31E. The E22G and F20E mutations are chosen because they have distinct and opposite effects on aggregation. The E22G mutation is associated with the familial Arctic form of AD[30] and enhances aggregation, whereas F20E Aβ42 shows a markedly reduced aggregation propensity compared with Aβ42.[9] For E22G/I31E Aβ42, it is important to distinguish between fibril and protofibril formation. Its fibril formation propensity was found to be almost as high as that of the E22G variant, whereas its propensity for forming protofibrils was found to be almost as low as that of the F20E variant.[9]

METHODS

Potential

We use an implicit solvent all-atom potential and allow only torsional degrees of freedom. A detailed description of the interaction potential can be found elsewhere.[31,32] Briefly, it is composed of four major terms:

$$E = E_{\mathrm{loc}} + E_{\mathrm{ev}} + E_{\mathrm{hb}} + E_{\mathrm{sc}}\,. \qquad (1)$$

The first term, E_{loc}, contains local interactions between atoms separated by only a few covalent bonds. The other three terms are nonlocal in character: E_{ev} represents excluded-volume effects, E_{hb} is a hydrogen-bond potential, and E_{sc} contains residue-specific interactions between pairs of sidechains. The E_{sc} potential contains two components: effective hydrophobic attraction and interactions among charged sidechains.

Predicting the three-dimensional structure of an arbitrary natively folded protein is a challenge. Characterizing an on average unstructured polypeptide like Aβ42 is a different type of problem. Here in, the task is to identify relevant conformational (sub)ensembles and find their relative populations, rather than to single out one particular conformation. One fundamental and nontrivial requirement when studying a natively unfolded protein is that the computational model must not be biased toward either α-helix or β-sheet structure. The model above has previously been shown to capture both structural and thermal stability properties of a diverse set of peptides and small proteins,[32] for one and the same set of model parameters, which makes it well suited for our study. To avoid introducing unphysical biases, we study Aβ42 using the same potential, with unchanged parameters, as in the previous studies of other sequences.[32]

Simulation techniques

We study the folding properties of the four Aβ42 variants by MC simulations of the above model. The simulations are performed using simulated tempering,[33,34] and cover six simulation temperatures in the range 297–367 K. These temperatures are nominal; the temperature scale is calibrated against experimental Aβ data below. All runs are started from random initial conformations.

Three different conformational updates are used in the simulations: single-variable updates of sidechain and backbone angles, respectively, and biased Gaussian steps (BGS).[35] The BGS move is semilocal and updates up to eight consecutive backbone degrees of freedom in a manner that keeps the ends of the segment approximately fixed. The ratio of sidechain to backbone updates is the same at all temperatures, whereas the relative frequency of the two backbone updates depends on the temperature. At high temperatures, the single variable update is the only backbone update used, and at low temperatures, only BGS is used. At intermediate temperatures, both updates are used.

For each of the four Aβ42 variants, we performed a set of 10 independent runs, using the open source C++-package PROFASI.[36] Each run contains $16 \cdot 10^9$ elementary MC steps and required ~20 days of computing time on an Intel Xeon 5160 (3.0 GHz) processor. The initial $2 \cdot 10^9$ MC steps of each run are discarded for thermalization.

Figure 1 illustrates the MC evolution of the energy E in one of the 10 runs for WT Aβ42. The figure also indicates how the temperature, a dynamical variable in simulated tempering, fluctuates during the run. During the course of the run, the system makes many independent visits to folded low-energy conformations, which is necessary to be able to estimate the relative populations of different folded states.

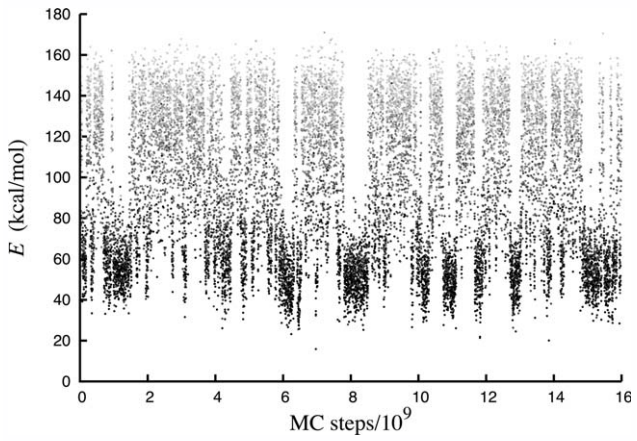

Figure 1

Monte Carlo (MC) evolution of the energy E in a typical run for wild type (WT) Aβ42. In the simulated-tempering method, the temperature is a dynamical variable. To indicate how the temperature fluctuates during the course of the simulation, data points corresponding to lower temperatures have been made darker.

Analysis

In the simulations, we monitor properties at different levels of detail. Secondary-structure content is measured using the program STRIDE.[37] The accessible hydrophobic surface area, HSA, is calculated using the algorithm by Shrake and Rupley[38] with 2000 test points. Atomic radii and probe radius are set according to Ooi *et al.*[39] All carbon atoms are defined as nonpolar and all other heavy atoms as polar.[40] Hydrogen atoms are excluded from the HSA calculation. A contact between two residues, which are not nearest or next-nearest neighbors along the chain, is defined as follows. A pair of heavy atoms within 4.5 Å of each other, one from each residue, is said to provide a link between the residues. The residues are defined as being in contact if there exist at least two links between them.

To identify structures formed by the central 17–32 segment, the generated conformations are clustered with respect to hydrogen bonds within this region. Here in every conformation is represented by a binary string in which every possible backbone hydrogen bond is assigned a status, either on or off, based on an energy cutoff. The states are clustered using the QT algorithm[41] with Hamming distance 2 as cluster diameter.

Temperature calibration

The temperature scale of the model we use was set using ~20-residue peptides[32] and turns out to require recalibration when studying the significantly larger Aβ. For this purpose, we compute J-coupling constants and chemical shifts from the simulations, which can be compared with experimental data.

In the J-coupling analysis, we compare with a set of 21 experimental $^3J(H_N,H_\alpha)$ values, determined by Sgourakis *et al.*[16] at 273 K and used by these authors to test several different force fields. We compute J-couplings for simulated conformations by using the Karplus equation[42] with coefficients derived by Schmidt *et al.*[43] The shape of the simulated data turns out to agree best with experimental data at our next-lowest temperature, nominally 310 K. Figure 2 shows our (ensemble averaged) simulated values at this temperature along with the experimental results. Although there are a few outlier points, the overall shapes of the two curves are in good agreement. The correlation coefficient is 0.57 when calculated over all the 21 couplings ($\lesssim$0.5 for the force fields tested by Sgourakis et al.[16]), and increases to 0.86 if four outliers (residues 2, 16, 21, and 22) are omitted.

Our chemical shift calculations are performed using the SHIFTS program,[44] and the results are compared with experimental C_α, C_β, and H_α data determined by Hou *et al.*[10] at 278 K. For the comparison with experimental data, we convert our (ensemble averaged) chemical shifts into a ternary chemical shift index (CSI; −1, 0, or 1),[45] measuring deviations from random coil values. As random coil values, we use the results at our highest simulation temperature, at which the random coil state dominates completely. Precisely as in the J-coupling case, the agreement with experimental data is best at the next-lowest simulation temperature. Figure 3 depicts our simulated CSI values at this temperature as well as the experimental results. Both data sets contain a similar amount of strand-indicating CSI values, and zero or few helix-indicating CSI values. There are also similarities in the locations of the strand-indicating CSI values. The three sets of experimental values themselves have no clear consensus.

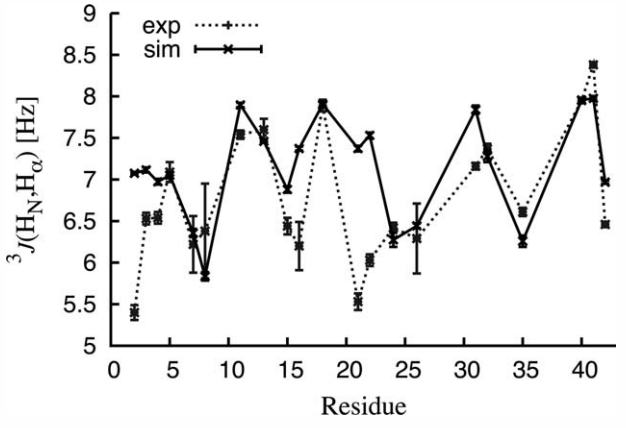

Figure 2

Experimental[16] (dots) and simulated (solid line) $^3J(H_N,H_\alpha)$-coupling constants.

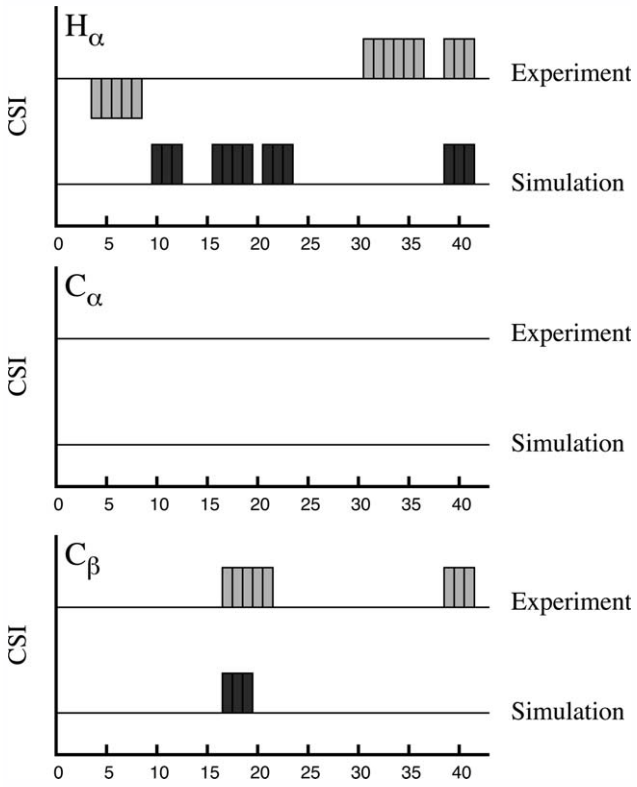

Figure 3

Experimental[10] and simulated H_α, C_α and C_β CSI values (see text). H_α and C_β CSI values of −1 and 1 indicate helix and strand, respectively.

In what follows, we will focus on the properties of A β at the next-lowest simulation temperature, at which the agreement with experimental *J*-couplings and chemical shifts is best. This simulation temperature should correspond to a physical temperature of ∼273–278 K.

RESULTS

Overall characterization

To characterize the conformational ensembles populated by the four Aβ42 variants, we begin by studying the free energy *F*(HSA,β), calculated as a function of hydrophobic surface area, HSA, and β-strand content, β. Figure 4 shows this free energy for all four sequences. For WT, there are two shallow but discernable free-energy minima of similar depth. One of the minima has higher HSA and higher β and corresponds to structures with single, extended β-sheets. The other minimum is of lower HSA and β, and the structures are more compact, often with two layers shielding a hydrophobic core. Examples of WT structures from the two minima are shown in Figure 4. For the mutant peptides, the structures found in these two regions of the (HSA, β)-plane are similar to those of WT — the difference lies in the balance between the minima. The F20E mutation increases the population of the high-HSA state, at the expense of the low-HSA state. The E22G/I31E mutation instead favors the state with lower HSA and lower β. The E22G mutation only marginally changes the relative population of the two states but lowers the barrier between them. For all four sequences, there is also a horizontal band of significantly populated low-β states.

Secondary-structure profiles

Figure 5 shows secondary-structure profiles for the four sequences. The α-helix probability varies smoothly along the sequence and is small (<0.15) everywhere, for all variants. The β-strand probability is significantly higher than the α-helix probability for most residues, but varies widely along the chain. A region of high β-strand probability is residues 17–19, which is part of the CHC. Comparing the different sequences, we see that their β-strand profiles share a similar overall shape. For example, all profiles show

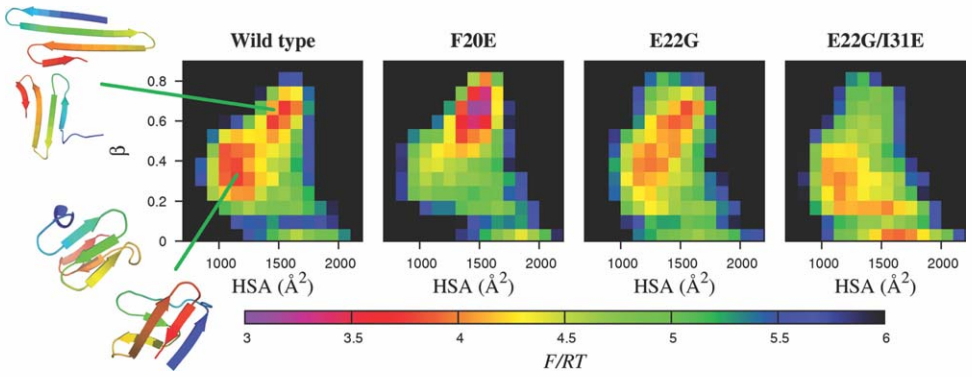

Figure 4

Free energy *F*(HSA,β), calculated as a function of hydrophobic surface area, HSA, and β-strand content, β, for the four Aβ42 variants. For WT Aβ42, two representative conformations (drawn with PyMOL[46]) are shown for each of the two major minima observed. The N- and C-terminal strands are colored blue and red, respectively.

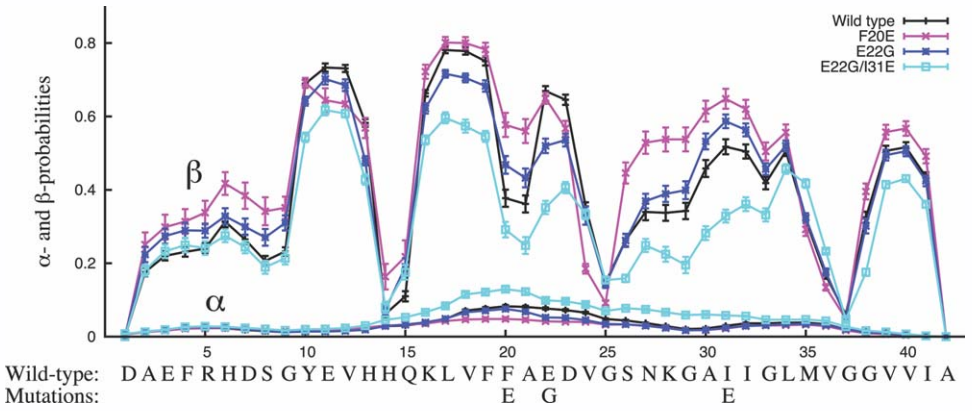

Figure 5

Secondary-structure profiles for the four Aβ42 variants. The probabilities of each residue to participate in α and β secondary structure were measured using STRIDE.[37] The WT amino acid sequence and the positions of the different mutations studied are indicated along the *x*-axis.

three sharp minima near residues 14, 25, and 37, respectively. These minima correspond to turn regions, as will be confirmed below. Although the overall shape of the profiles is similar, some interesting differences can also be seen. The main differences are found in the 17–32 segment. Perhaps somewhat surprising are the effects of the mutation F20E. Naively, one might expect the loss of the strongly hydrophobic F20 to have a destabilizing effect on the overall structure and thereby lead to a reduced β-strand content. In addition, glutamic acid has a high helix-forming propensity. Note, therefore, that we find that this mutation leads to a significant increase in β-strand probability for residues 20, 21, and 26–29.

Contact maps

To elucidate the tertiary organization of the peptides, we construct contact maps, which display the probabilities of contact formation for all possible residue pairs (except nearest and next-nearest neighbors). Figure 6 shows our calculated contact maps. For WT, most of the frequent contacts are found within the four chain segments 4–12, 9–20, 17–32, and 28–42. Three major bands of populated contacts can be seen, all extending perpendicularly from the diagonal. These bands correspond to bend structures, centered at residues 13–16, 23–26, and 35–38, respectively. These turn regions coincide with the three regions of low β-strand probability identified above (Figure 5).

In the contact maps, as in the secondary-structure profiles, the main effects of the mutations are found in the 17–32 region. A major part of the frequent contacts within this region are associated with the bend centered at residues 23–26. In addition, there is a smaller group of frequent contacts representing interactions between the CHC and residues 22–24. Several contacts in this second group are weakened by all the three mutations studied; examples

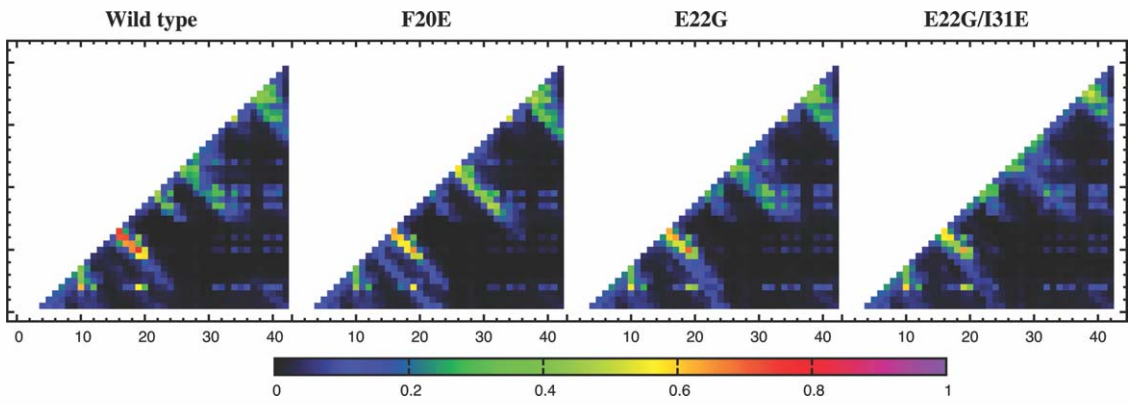

Figure 6

Probability map of residue contact formation for the four Aβ42 variants.

Table I
Turn Location and Populations (in %) for the Hairpins H1-5

Hairpin	Turn	WT	F20E	E22G	E22G/I31E
H1	20-21	29.8 ± 1.5	12.1 ± 1.3	10.9 ± 1.0	11.4 ± 0.5
H2	23-24	0.6 ± 0.2	4.4 ± 2.3	0.3 ± 0.2	0.2 ± 0.1
H3	24-25	18.6 ± 2.1	33.9 ± 3.3	15.3 ± 2.2	2.5 ± 0.4
H4	25-26	5.9 ± 0.8	3.1 ± 0.5	11.8 ± 2.4	9.2 ± 1.5
H5	25-26	1.4 ± 0.3	0.3 ± 0.1	3.4 ± 1.3	5.5 ± 1.4

of this are the (18,23) and (17,24) contacts. The bend centered at residues 23–26 is, by contrast, affected differently by different mutations. The F20E mutation makes this band of frequent contacts more narrow, which means that the conformational diversity of this structure is reduced. This finding is consistent with the above observation of an increased β-strand probability in this region for this mutant. The E22G mutation instead increases the conformational diversity of the bend. This effect is only barely visible in Figure 6 but can be clearly seen from the hairpin populations discussed below (Table I). The E22G/I31E mutation makes many contacts associated with the bend much weaker and therefore has a strongly destabilizing effect on this structure.

The 17–32 region

The conformational differences in the 17–32 region can be further elucidated by a cluster analysis with respect to hydrogen bonds within this segment (see Methods). This analysis identifies six major clusters, all of which are >3 % populated for at least one of the variants. In one of these clusters, the 17–32 segment is coil like. This cluster is the largest or next-largest one for all four variants (population 6–10%). The other five clusters correspond to different β-hairpins, labeled H1–5 and illustrated in Figure 7. Each of these hairpins can be characterized by a set of four or five hydrogen bonds (see Figure 7) and may also occur in other, less populated clusters. The population of a hairpin is therefore calculated as the fraction of all conformations in which at most one of its defining hydrogen bonds is missing. Table I shows the turn location and populations of the five hairpins. The mutations have some interesting effects on the hairpin populations. First, the population of H1, with its turn at residues 20 and 21, is reduced by all the mutations, which is consistent with the above observation that all three mutations weaken contacts between the CHC and residues 22–24. Second, the F20E mutation makes one of the hairpins, H3, dominate, which explains the reduced conformational diversity of this variant. Finally, we note that the E22G and E22G/I31E mutations, with enhanced fibril formation, increase the populations of H4 and H5, whose turns are close to the loop region of Aβ fibrils,[24,25] whereas the aggregation-decelerating F20E mutation reduces the populations of these hairpins.

The 17–32 segment also makes many other, less populated hairpins in the simulations, one of which occurs in the Aβ conformation selected by Affibody binders.[26] This hairpin has a population of ∼0.5 %, depending on Aβ42 variant.

DISCUSSION

The four Aβ42 variants studied all form a variety of compact and β-sheet rich structures in the simulations.

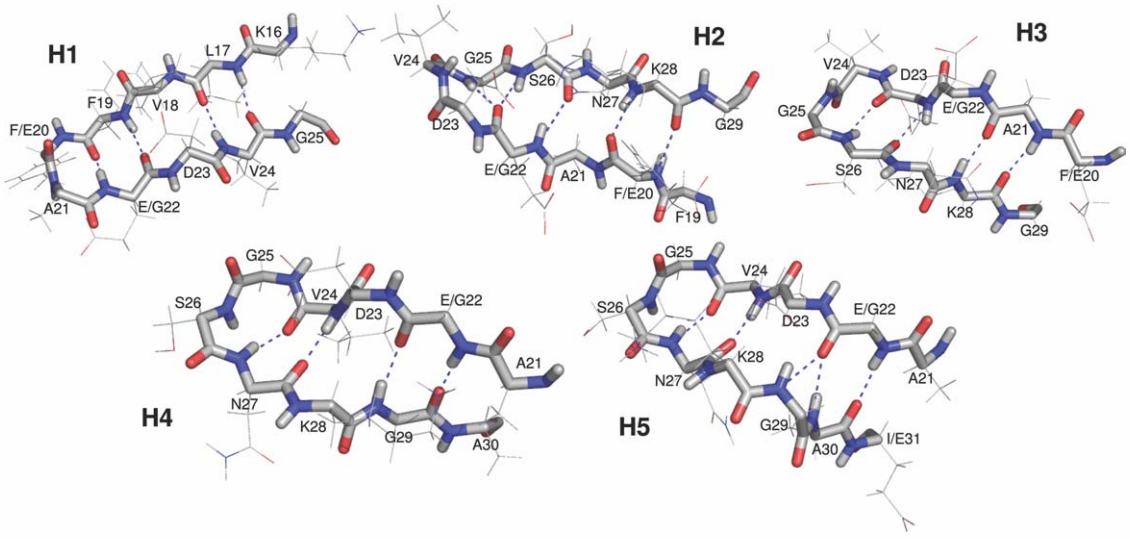

Figure 7
3D models of the hairpins H1–5 (drawn with PyMOL[46]). The hydrogen bonds used in the analysis of hairpin populations are shown as blue dashed lines.

Despite this diversity, two major families of conformations can be identified. One corresponds to single β-sheets and the other to more compact structures, typically with two layers. The simulated conformations further display three major turn regions, centered at residues 13–16, 23–26, and 35–38, respectively.

The 13–16 turn corresponds to a quite well-defined β-hairpin (Fig. 5 and 6). Closer inspection reveals that the formation of this hairpin puts the H13 and H14 sidechains on the same side of the backbone, which is interesting because the histidines H6, H13, and H14 are involved in the binding of Zn and Cu ions,[47,48] an interaction that might play a key role in AD.[49]

The 35–38 turn is conformationally more diverse than the 13–16 turn and does not correspond to a single β-hairpin but rather to a family of such structures (Fig. 5 and 6). Both these turns have in common that they are only weakly affected by the mutations studied.

The middle 23–26 turn is located in the 17–32 segment, where the mutational effects are strong. Within this segment, in addition to the 23–26 turn, there is also a small group of populated contacts between the CHC and residues 22–24. These contacts are weakened by all three mutations studied. A similar observation was made in recent simulations of Aβ(15–28), where the E22Q mutation, associated with familial Dutch AD, was found to weaken interactions between the CHC and a bend spanning residues 22–28.[50]

The response of the 23–26 turn to the mutations is intriguing. The E22G mutation increases the conformational diversity of this turn, which probably can be attributed to the high intrinsic flexibility of glycine and the loss of a favorable electrostatic interaction between E22 and K28. The F20E mutation instead decreases the conformational diversity of the same turn. The loss of the strongly hydrophobic and potentially stabilizing F20 does not prevent the formation of the turn but seems to reduce the number of competing low-energy conformations.

The opposite effects of these two mutations in the simulations are interesting, especially because the above-mentioned Drosophila study[9] found the F20E and E22G mutations to increase and decrease, respectively, fly longevity and locomotion. It is further known that the F20E and E22G mutations decelerate and accelerate, respectively, the *in vitro* aggregation of Aβ42.[9] The different aggregation properties can probably be explained, at least partially, in terms of primary structure alone; the F20E mutation introduces a charged residue into the CHC region, whereas the E22G mutation removes a charged residue near the CHC. Do the mutations have additional effects on aggregation, stemming from altered folding properties? An experimental study of the effects of several disease-associated mutations on Aβ(21–30) suggests that this might be the case.[22] All these mutations destabilized the bend structure that this fragment adopts in solution,[18] and the destabilizing effect of a mutation was further found to correlate with its influence on full-length Aβ oligomerization.[22] Our finding that E22G Aβ42 shows an increased conformational diversity in the 23–26 region is perfectly in line with these results. Interestingly, the same picture seems to hold for the F20E mutation as well. Experiments found that this mutation decelerates aggregation,[9] and we find that it reduces the conformational diversity in this region.

The strongly reduced population of the 23–26 turn that we observe for E22G/I31E Aβ42 does not conform with this picture, because this variant does not aggregate faster than E22G Aβ42.[9] It is possible that the double mutation affects the free-energy landscape too much for this simple picture to remain valid. The fact that E22G/I31E Aβ42 has been found to have a high global aggregation propensity but only a low propensity for forming protofibrils[9] may indicate that the aggregation mechanisms indeed are different for this variant.

In fibrils, each Aβ42 molecule is believed to exhibit a loop located near in sequence to the 23–26 region.[25,51,52] A 23–26 turn is, however, not identical to the fibril loop, but has to be reorganized upon fibril formation. Increased conformational diversity should facilitate such a reorganization, which provides a possible explanation of how turn destabilization might lead to faster aggregation.[22] It is also worth noting that the formation of a 23–26 turn may lead to a partial protection of the CHC from the solvent. Turn destabilization may therefore increase the solvent exposure of the CHC, which is another possible aggregation-accelerating mechanism.

The reduced diversity of the 23–26 turn observed for the slowly aggregating F20E variant implies a reduced access for this mutant to conformations that might be favorable for aggregation. It is therefore interesting to note that this mutation leads to a suppression of the H4 and H5 hairpins, which are instead enhanced by the E22G and E22G/I31E mutations, both of which speed up fibril formation.

Although we are unaware of any previous simulations of all the four Aβ42 variants studied here, there have been many studies of the WT sequence. A turn in the 23–26 region was observed in several WT studies based on completely different computational models,[16,17,53] which indicates that our observation of this turn is not a model artifact.

A difference between our and most previous WT Aβ42 simulations[13–17,54] is in the overall strand content, which is higher in our case. From our comparisons with experimental *J*-couplings and chemical shifts, we see no sign that this higher sheet content would be an overestimate. The agreement with experimental data is poor at the simulation temperatures where the strand content is lower; the number of strand-indicating simulated CSI values gets too low and the shape of the *J*-coupling data gets too flat, compared with experimental data.

Still, the comparisons with experimental data cannot completely rule out possible biases of the force field toward, for example, strand structure. It should therefore be stressed that we expect many hypothetical biases to cancel out when studying differences among the peptides. Relative properties are likely to be less sensitive than absolute properties to force field details.

This study has focused on Aβ42, the Aβ form most closely linked to AD. How a truncation to Aβ40 would change our results is difficult to say. Although experiments indicate that the main conformational differences between Aβ40 and Aβ42 are found at the C terminus,[10,12] it is possible that the truncation also affects, for example, the 23–26 turn.

CONCLUSIONS

We have investigated the folding properties of WT Aβ42 and three variants that are markedly different from each other and from the WT sequence in terms of aggregation properties. We find that the three mutations alter the global folding free-energy landscape of Aβ42 and in particular have a significant impact on a turn region at residues 23–26. The E22G/I31E variant, with heterogeneous aggregation properties,[9] is found to have a reduced overall probability of forming turns at all in this region. Our simulations of the Arctic E22G variant support the hypothesis that reduced stability of this turn speeds up aggregation.[22] This picture is extended by our results for the slowly aggregating F20E variant, which is found to instead decrease the conformational diversity of the turn. This reduced diversity entails a suppression of turn conformations that are readily accessible to the other variants and might be essential in aggregation.

ACKNOWLEDGMENT

We thank Giorgio Favrin for helpful discussions. This work was in part supported by the Swedish Research Council.

REFERENCES

1. Dahlgren KN, Manelli AM, Stine WB, Jr, Baker LK, Krafft GA, Ladu MJ. Oligomeric and fibrillar species of amyloid-β peptides differentially affect neuronal viability. J Biol Chem 2002;277:32046–32053.
2. Selkoe DJ. Translating cell biology into therapeutic advances in Alzheimer's disease. Nature 1999;399:A23–A31.
3. Zhang Y, McLaughlin R, Goodyer C, LeBlanc A. Selective cytotoxicity of intracellular amyloid β peptide$_{1–42}$ through p53 and Bax in cultured primary human neurons. J Cell Biol 2002;156:519–529.
4. Bitan G, Kirkitadze MD, Lomakin A, Vollers SS, Benedek GB, Teplow DB. Amyloid-β protein (Aβ) assembly: Aβ40 and Aβ42 oligomerize through different pathways. Proc Natl Acad Sci USA 2003;100:330–335.
5. Harper JD, Wong SS, Lieber CM, Lansbury PT. Observation of metastable Aβ amyloid protofibrils by atomic force microscopy. Chem Biol 1997;4:119–125.
6. Jarrett JT, Berger EP, Lansbury PT, Jr. The carboxy terminus of the β amyloid protein is critical for the seeding of amyloid formation: implications for the pathogenesis of Alzheimer's disease. Biochemistry 1993;32:4693–4697.
7. Walsh DM, Lomakin A, Benedek GB, Condron MM, Teplow DB. Amyloid β-protein fibrillogenesis. Detection of a protofibrillar intermediate. J Biol Chem 1997;272:22364–22372.
8. Iijima K, Chiang HC, Hearn SA, Hakker I, Gatt A, Shenton C, Granger L, Leung A, Iijima-Ando K, Zhong Y. Aβ42 mutants with different aggregation profiles induce distinct pathologies in Drosophila. PLoS One 2008;3:e1703.
9. Luheshi LM, Tartaglia GG, Brorsson A, Pawar AP, Watson IE, Chiti F, Vendruscolo M, Lomas DA, Dobson CM, Crowther DC. Systematic in vivo analysis of the intrinsic determinants of amyloid β pathogenicity. PLoS Biol 2007;5:e290.
10. Hou L, Shao H, Zhang Y, Li H, Menon NK, Neuhaus EB, Brewer JM, Byeon IJL, Ray DG, Vitek MP, Iwashita T, Makula RA, Przybyla AB, Zagorski MG. Solution NMR studies of the Aβ40 and Aβ42 peptides establish that the Met35 oxidation state affects the mechanism of amyloid formation. J Am Chem Soc 2004;126:1992–2005.
11. Riek R, Güntert P, Döbeli H, Wipf B, Wüthrich K. NMR studies in aqueous solution fail to identify significant conformational differences between the monomeric forms of two Alzheimer peptides with widely different plaque-competence, Aβ40^{ox} and Aβ42^{ox}. Eur J Biochem 2001;268:5930–5936.
12. Yan Y, Wang C. Aβ42 is more rigid than Aβ40 at the C terminus: implications for Aβ aggregation and toxicity. J Mol Biol 2006;364:853–862.
13. Anand P, Nandel FS, Hansmann UHE. The Alzheimer's β amyloid (Aβ$_{1–39}$) monomer in an implicit solvent. J Chem Phys 2008;128:165102.
14. Baumketner A, Bernstein SL, Wyttenbach T, Bitan G, Teplow DB, Bowers MT, Shea JE. Amyloid β-protein monomer structure: a computational and experimental study. Protein Sci 2006;15:420–428.
15. Flöck D, Colacino S, Colombo G, di Nola A. Misfolding of the amyloid β-protein: a molecular dynamics study. Proteins 2006;62:183–192.
16. Sgourakis NG, Yan Y, McCallum SA, Wang C, García AE. The Alzheimer's peptides Aβ40 and 42 adopt distinct conformations in water: a combined MD/NMR study. J Mol Biol 2007;368:1448–1457.
17. Yang M, Teplow DB. Amyloid β-protein monomer folding: free-energy surfaces reveal alloform-specific differences. J Mol Biol 2008;384:450–464.
18. Lazo ND, Grant MA, Condron MC, Rigby AC, Teplow DB. On the nucleation of amyloid β-protein monomer folding. Protein Sci 2005;14:1581–1596.
19. Baumketner A, Bernstein SL, Wyttenbach T, Lazo ND, Teplow DB, Bowers MT, Shea JE. Structure of the 21–30 fragment of amyloid β-protein. Protein Sci 2006;15:1239–1247.
20. Chen W, Mousseau N, Derreumaux P. The conformations of the amyloid-β (21–30) fragment can be described by three families in solution. J Chem Phys 2006;125:084911.
21. Cruz L, Urbanc B, Borreguero JM, Lazo ND, Teplow DB, Stanley HE. Solvent and mutation effects on the nucleation of amyloid β-protein folding. Proc Natl Acad Sci USA 2005;102:18258–18263.
22. Grant MA, Lazo ND, Lomakin A, Condron MM, Arai H, Yamin G, Rigby AC, Teplow DB. Familial Alzheimer's disease mutations alter the stability of the amyloid β-protein monomer folding nucleus. Proc Natl Acad Sci USA 2007;104:16522–16527.
23. Krone MG, Baumketner A, Bernstein SL, Wyttenbach T, Lazo ND, Teplow DB, Bowers MT, Shea JE. Effects of familial Alzheimer's disease mutations on the folding nucleation of the amyloid β-protein. J Mol Biol 2008;381:221–228.
24. Petkova AT, Ishii Y, Balbach JJ, Antzutkin ON, Leapman RD, Delaglio F, Tycko R. A structural model for Alzheimer's β-amyloid fibrils based on experimental constraints from solid state NMR. Proc Natl Acad Sci USA 2002;99:16742–16747.

25. Lührs T, Ritter C, Adrian M, Riek-Loher D, Bohrmann B, Döbeli H, Schubert D, Riek R. 3D structure of Alzheimer's amyloid-β(1–42) fibrils. Proc Natl Acad Sci USA 2005;102:17342–17347.
26. Hoyer W, Grönwall C, Jonsson A, Ståhl S, Härd T. Stabilization of a β-hairpin in monomeric Alzheimer's amyloid-β peptide inhibits amyloid formation. Proc Natl Acad Sci USA 2008;105:5099–5104.
27. Grönwall C, Jonsson A, Lindstrom S, Gunneriusson E, Ståhl S, Herne N. Selection and characterization of Affibody ligands binding to Alzheimer amyloid β peptides. J Biotechnol 2007;128:162–183.
28. Balbach JJ, Ishii Y, Antzutkin ON, Leapman RD, Rizzo NW, Dyda F, Reed J, Tycko R. Amyloid fibril formation by Aβ(16–22), a seven-residue fragment of the Alzheimer's β-amyloid peptide, and structural characterization by solid state NMR. Biochemistry 2000; 39:13748–13759.
29. Tjernberg LO, Näslund J, Lindqvist F, Johansson J, Karlström AR, Thyberg J, Terenius L, Nordstedt C. Arrest of β-amyloid fibril formation by pentapeptide ligand. J Biol Chem 1996;271:8545–8548.
30. Nilsberth C, Westlind-Danielsson A, Eckman CB, Condron MM, Axelman K, Forsell C, Stenh C, Luthman J, Teplow DB, Younkin SG, Näslund J, Lannfelt L. The 'Arctic' APP mutation (E693G) causes Alzheimer's disease by enhanced Aβ protofibril formation. Nat Neurosci 2001;4:887–893.
31. Irbäck A, Mohanty S. Folding thermodynamics of peptides. Biophys J 2005;88:1560–1569.
32. Irbäck A, Mitternacht S, Mohanty S. An effective all-atom potential for proteins. PMC Biophys 2009;2:2.
33. Lyubartsev AP, Martsinovski AA, Shevkunov SV, Vorontsov-Velyaminov PN. New approch to Monte Carlo calculation of the free energy: Method of expanded ensembles. J Chem Phys 1992;96: 1776–1783.
34. Marinari E, Parisi G. Simulated tempering: a new Monte Carlo scheme. Europhys Lett 1992;19:451–458.
35. Favrin G, Irbäck A, Sjunnesson F. Monte Carlo update for chain molecules: Biased Gaussian steps in torsional space. J Chem Phys 2001;114:8154–8158.
36. Irbäck A, Mohanty S. PROFASI: a Monte Carlo simulation package for protein folding and aggregation. J Comput Chem 2006;27:1548–1555.
37. Frishman D, Argos P. Knowledge-based protein secondary structure assignment. Proteins 1995;23:566–579.
38. Shrake A, Rupley JA. Environment and exposure to solvent of protein atoms. Lysozyme and insulin. J Mol Biol 1973;79:351–371.
39. Ooi T, Oobatake M, Némethy G, Scheraga HA. Accessible surface areas as a measure of the thermodynamic parameters of hydration of peptides. Proc Natl Acad Sci USA 1987;84:3086–3090.
40. Miller S, Janin J, Lesk AM, Chothia C. Interior surface of monomeric proteins. J Mol Biol 1987;196:641–656.
41. Heyer LJ, Kruglyak S, Yooseph S. Exploring expression data: identification and analysis of coexpressed genes. Genome Res 1999;9: 1106–1115.
42. Karplus M. Contact electron-spin coupling of nuclear magnetic moments. J Chem Phys 1959;30:11–15.
43. Schmidt JM, Blümel M, Löhr F, Rüterjans H. Self-consistent ^{3}J coupling analysis for the joint calibration of karplus coefficients and evaluation of torsion angles. J Biomol NMR 1999;14:1–12.
44. Xu XP, Case DA. Automated prediction of ^{15}N, $^{13}C^{\alpha}$, $^{13}C^{\beta}$ and $^{13}C^{\beta}$ chemical shifts in proteins using a density functional database. J Biomol NMR 2001;21:321–333.
45. Wishart DS, Sykes BD, The ^{13}C chemical-shift index: a simple method for the identification of protein secondary structure using ^{13}C chemical shift data. J Biomol NMR 1994;4:171–180.
46. DeLano WL. The PyMOL molecular graphics system, San Carlos, CA: DeLano Scientific; 2002.
47. Curtain CC, Ali F, Volitakis I, Cherny RA, Norton RS, Beyreuther K, Barrow CJ, Masters CL, Bush AI, Barnham KJ. Alzheimer's disease amyloid-β binds copper and zinc to generate an allosterically ordered membrane-penetrating structure containing superoxide dismutase-like subunits. J Biol Chem 2001;273:20466–20473.
48. Syme CD, Nadal RC, Rigby SEJ, Viles JH. Copper binding to the amyloid-beta (Aβ) peptide associated with Alzheimer's disease: folding, coordination geometry, pH dependence, stoichiometry, and affinity of Aβ-(1–28): insights from a range of complementary spectroscopic techniques. J Biol Chem 2004;279:18169–18177.
49. Bush AI. The metallobiology of Alzheimer's disease. Trends Neurosci 2003;26:207–214.
50. Baumketner A, Krone MG, Shea JE. Role of familial dutch mutation E22Q in the folding and aggregation of the 15–28 fragment of the Alzheimer amyloid-β protein. Proc Natl Acad Sci USA 2008; 105:6027–6032.
51. Olofsson A, Sauer-Eriksson AE, Öhman A. The solvent protection of Alzheimer amyloid-β-(1–42) fibrils as determined by solution NMR spectroscopy. J Biol Chem 2006;281:477–483.
52. Masuda Y, Uemura S, Ohashi R, Nakanishi A, Takegoshi K, Shimizu T, Shirasawa T, Irie K. Identification of physiological and toxic conformations in Aβ aggregates. ChemBioChem 2009;10:287–295.
53. Lam AR, Teplow DB, Stanley HE, Urbanc B. Effects of the arctic ($E^{22} \rightarrow G$) mutation on amyloid β-protein folding: discrete molecular dynamics study. J Am Chem Soc 2008;130:17413–17422.
54. Melquiond A, Dong X, Mousseau N, Derreumaux P. Role of the region 23–28 in Aβ fibril formation: insights from simulations of the monomers and dimers of Alzheimer's peptides Aβ40 and Aβ42. Curr Alzheimer Res 2009;5:244–250.